Segmenting the prostate and rectum in CT imagery using anatomical constraints

Siqi Chen, D. Michael Lovelock, and Richard J. Radke

Abstract

The automatic segmentation of the prostate and rectum from 3-D computed tomography (CT) images is still a challenging problem, and is critical for image-guided therapy applications. We present a new, automatic segmentation algorithm based on deformable organ models built from previously segmented training data. The major contributions of this work are a new segmentation cost function based on a Bayesian framework that incorporates anatomical constraints from surrounding bones and a new appearance model that learns a nonparametric distribution of the intensity histograms inside and outside organ contours. We report segmentation results on 185 datasets of the prostate site, demonstrating improved performance over previous models.

Index Terms

Deformable segmentation, prostate and rectum, segmentation, shape and appearance model, image-guided radiation therapy.

I. INTRODUCTION

Intensity–modulated radiotherapy (IMRT), an exciting recent technology for cancer treatment, can target a high dose of radiation to tumors while limiting the dose to surrounding healthy organs. The accurate segmentation of the target and surrounding radiation-sensitive organs from a three-dimensional planning scan is critical for achieving high-quality radiation plans; this problem is often called contouring. Contours are traditionally generated manually by physicians; however, the process is time-consuming and the intra- and inter-observer variation in contouring can be large [7]. Developing automatic segmentation tools is important for accelerating treatment planning and making the contouring process repeatable and accurate.

Model-based algorithms are increasingly successful for medical image segmentation, since they are robust to low signal-to-noise ratio, poor image contrast and organ deformations. Models built and learned from real training data are critical for the successful segmentation of organs, especially those whose shapes vary widely across the population. In this paper, we are specifically interested in the automatic segmentation of organs in the male pelvic cavity, such as the prostate and rectum, for the purpose of radiotherapy treatment planning. Segmenting the prostate and rectum from 3D CT imagery is difficult for two main reasons, as illustrated in Figure 1.
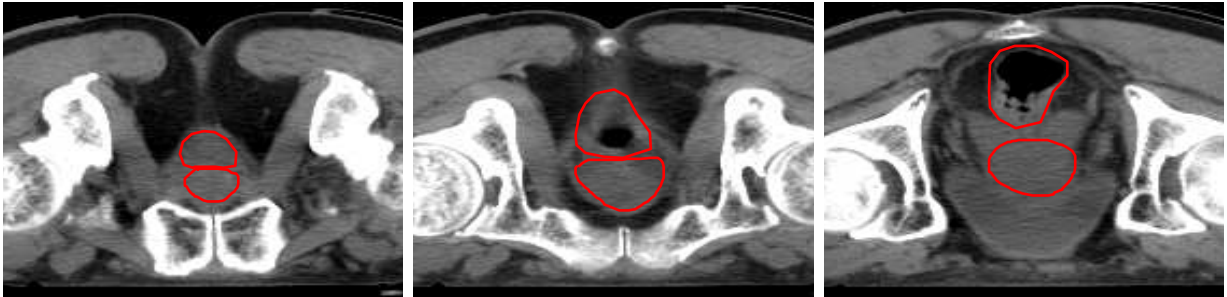

Fig. 1. Ground truth contours of the prostate (bottom contour) and rectum (top contour) from different axial slices of a 3D CT scan, illustrating the challenges of automatic segmentation.

1) There is frequently little to no intensity difference between the prostate, bladder and surrounding muscles. Standard edge-based deformable segmentation algorithms (e.g., snakes) are likely to fail in the absence of a shape model.

2) Due to gas and filling, the rectum has an inhomogeneous, unpredictable intensity distribution. The mean and variance of the pixels in the rectum interior are likely to be an inadequate basis for segmentation.

Our approach to these challenges is to build point-based active shape models for the prostate and rectum, using a library of expert-contoured CT scans. We extend our previous model-based segmentation approach [14] in several ways. First, we introduce new anatomical constraints that prevent the shape model from extending into physically unrealistic configurations, based on automatic pre-segmentation of the pelvic bones. Second, to overcome the challenge of appearance variability, we retain the training segmentations' histograms as the basis for learning an accurate distribution of the intensities inside and outside the desired contours for a new scan. Third, we propose a new cost function that incorporates a shape cost, an anatomy cost and an intensity cost into a Bayesian estimation framework. Taken together, these innovations improve

the segmentations achievable with our approach by several percentage points of detection and false alarm probabilities.

The remainder of the paper is organized as follows. In Section II, we briefly review related work on model-based image segmentation, especially for the pelvic site. Section III explains how we automatically extract pelvic bone boundaries from the CT images to guide the segmentation. Section IV reviews our method for constructing a parametric 3D shape model. In Section V, we describe a new segmentation algorithm that leverages the anatomical constraints. Results of prostate and rectum segmentation are presented in Section VI. Finally, we conclude and discuss possible directions of future research in Section VII.

II. RELATED PRIOR WORK ON MODEL-BASED IMAGE SEGMENTATION

In this section, we briefly overview related work on medical image segmentation. For more information, we refer the readers to an excellent recent survey [22].

A. Shape Representation

Choosing an appropriate shape representation is the first problem in statistical model-based segmentation. The choices can be broadly classified as explicit shape representations and implicit shape representations. The simplest and most straightforward explicit method is to represent a shape by a set of points sampled across its surface, which are often referred to as *landmarks* in the literature. Cootes et al. [9] introduced the groundbreaking statistical shape modeling approach called "active shape models" (ASM), which are based on point-based shape representations. Pizer et al. [38] proposed to model shapes with medial representations called *m-reps*. Staib and Duncan [43] applied Fourier analysis to describe shapes of different topologies. Spherical harmonic shape representations (SPHARM) [27] and spherical wavelet transforms [35] were also proposed as shape representations for medical image segmentation.

As an alternative to explicit shape representations, implicit shape representations based on level sets have recently attracted much attention. In this approach, a shape is determined by the zero level set of a higher-dimensional embedding function ϕ such as a signed distance function (SDF) [37]. Leventon et al. [29] proposed seminal work to perform Principal Component Analysis (PCA) on a set of training SDFs.

B. The Correspondence Problem

In statistical shape models, well-defined correspondences must be established between train-ing shapes before statistical analysis such as PCA can be applied. Manually determining the correspondences is time consuming, difficult to reproduce, and can be very challenging in 3D cases. Thus, it is important to automatically obtain unbiased and consistent correspondences, so that a model can capture the desired statistical characteristics of shape variability. However, in general, this is an extremely difficult problem.

Much work has been proposed to solve the correspondence problem for point-based shape representations. Chui et al. [6] described an annealing based joint clustering and matching technique to establish correspondences. This approach was extended by Wang et al. [46] who used the Jensen-Shannon divergence measure to non-rigidly register multiple unlabeled point sets. Davies et al. [12] solved the correspondence problem by minimizing the Minimum Description Length (MDL) of a shape ensemble. However, most of these approaches are very time consuming, and therefore may not be appropriate for radiotherapy applications. Recently, Jeong and Radke [25] proposed a simple and effective way of finding reasonable correspondences for pelvic organs. We use this approach in our work. In most methods, an initial rough alignment (e.g., a similarity transformation) may be estimated before establishing the correspondences, although this step is not required for our dataset as discussed in Section IV.

C. Model Construction

Once the correspondence is established, statistical analysis is performed over the corresponding points to create a model. Principal Component Analysis (PCA) is frequently applied to model the shape variation [9]. Further techniques were developed to enhance the capability of the model to capture the nonlinear aspects of shape variation such as kernel PCA [39] and bilinear models [16].

Apart from point based shape representations, direct PCA on the space of SDFs was also proposed by Leventon et al. [29] and Tsai et al. [44]. However, this approach has the limitation that since the space of SDFs is not linear, neither the mean level set nor a linear combination of eigenmodes will correspond to a valid SDF. Cremers et al. [11] recently described how kernel density estimation technique could be applied to level set functions.

D. Appearance Models

Once the shape model is built, image intensities must be incorporated into the segmentation. Many algorithms are based on simple intensity gradients or the statistics of both the inside and outside of a closed contour to direct the movement of the curve to the edge of an object [26], [4]. These formulations are reasonable for segmentation tasks where the regions of interest are characterized by distinct and roughly homogeneous intensities. However, in most medical image segmentation problems, such assumptions may no longer hold and incorporating learned intensity information from the training images is a better approach.

One class of algorithms is based on intensity features along the boundary of the object of interest. Cootes et al. [9] used intensity samples along the profiles perpendicular to the surface of training images to build a PCA model for each landmark. Brejl and Sonka [2] combined the intensity and gradient profiles into a large feature vector.

Another class of algorithms uses the intensity information of regions inside and outside the object of interest to drive the segmentation. The "active appearance model" introduced in [8] transforms the training shapes to a reference shape and uses all pixel intensities to build a feature vector. PCA was applied to the joint shape-intensity training vectors as the basis for a segmentation cost function. However, the huge dimension required to store every interior intensity pixel of the object is very challenging, particularly for 3D segmentation problems [34]. One approach is to use the intensity distribution, such as the normalized histogram, to drive the segmentation; our method falls into this category. Freedman et al. [14] learned a reference interior histogram from training images and formulated a cost function based on the distance between the evolving and reference histograms. However, robustly learning the reference histogram was problematic. Broadhurst et al. [3] mapped the inside and outside histograms to Euclidean space using the earth mover's distance and characterized the variation of the histograms with a Gaussian model.

E. Prior Work on Pelvic Organ Segmentation

Despite the difficulty of segmenting pelvic organs like the prostate, rectum and bladder, several semi-automatic (e.g., [23]) and automatic methods have been proposed. We classify these approaches in the following way:

1) Model-based methods: Due to their ability to learn prior information from training images, model-based segmentation algorithms have been applied extensively to the pelvic site. We previously proposed linear [14] and bilinear [24] models for segmenting CT prostate images. Freedman and Zhang [15] devised a semi-automatic graph-cut bladder segmentation algorithm using shape priors. Rousson et al. [40] proposed a level-set based Bayesian segmentation framework that incorporated an intensity cost and a shape cost. Broadhurst et al. [3] used an "m-rep" shape representation along with a multi-scale approach to segment the bladder, prostate and rectum. Costa et al. [10] employed a non-overlapping constraint for coupled segmentation of the prostate and bladder with deformable models. Gibou et al. [18] used a piecewise level-set based Mumford-Shah model to segment the bladder and rectum. Tsai et al. [44] proposed to combine various region-based segmentation methods with the PCA-based level-set shape model to segment pelvic organs from MRI.

2) Registration-based methods: Foskey et al. [13] and Smitsmans et al. [42] both proposed bony-pelvis-based image registration as the basis for deforming prostate contours from a training image to match a new image. Martin et al. [31] presented a hybrid registration method which coupled an intensity-based registration with a robust point-matching algorithm. Klein et al. [28] described a nonrigid registration-based atlas matching technique to segment the prostate. Other non-rigid registration methods include joint CT bladder registration and segmentation [45] and fast block-matching-based CT prostate elastic registration [30].

3) Other approaches: Zaim et al. [48] proposed a Kohonen clustering network approach using feature-based measures of the gray-level co-occurrence matrix (GLCM) for segmenting the prostate. Other approaches include region-growing methods ([32], [20]), genetic algorithms [17], radial searching [47], and polar transformation based methods [49].

III. ANATOMICAL CONSTRAINTS FOR SEGMENTATION

The male pelvic cavity is composed of the pelvis, the sacrum, the coccyx and the pubic symphysis. The prostate gland is located in the pelvic cavity, behind the pubic symphysis and pubic arch. The pubic arch is formed by the convergence of the inferior rami of the ischium and pubis of each side, which we will term as the front pelvis bones. The prostate is also located in front of the neck of the bladder, and above the rectum. The rectum is a slightly S-shaped organ located in front of the coccyx and behind the prostate and bladder. Given this pelvic structure,

we know that the prostate and rectum should be found within a region bounded by the front, left, and right pelvis bones and the coccyx. Our approach is to use the automatic pre-localization of these objects to guide the segmentation of the prostate and the rectum.
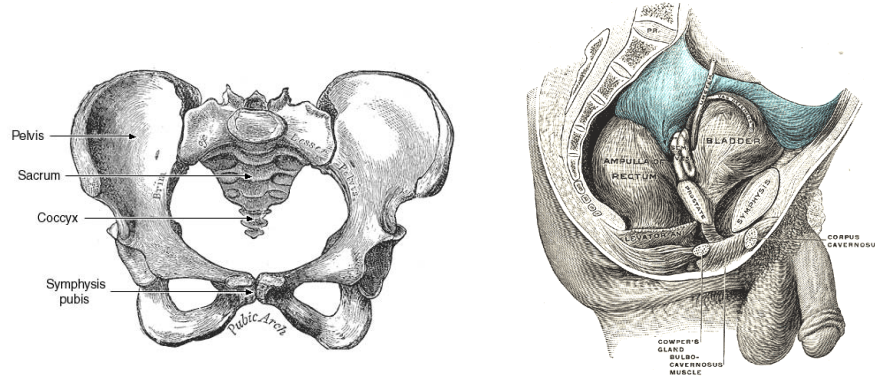

Fig. 2.   The anatomical structure of pelvic organs (from [19]).

As mentioned above, other researchers have noted the usefulness of pelvic bony structures for soft-tissue organ localization and segmentation. Since their positions and shapes are fundamentally fixed during radiation treatment, bony structures have been used to design deformable image registration techniques that were shown to be highly effective for tracking internal organ changes and compensating for set-up errors in image-guided adaptive radiation therapy [1]. Although some registration-based algorithms discussed in Section II linked the segmentation of pelvic organs to the localization of pelvic bony structures, we note that they are not direct segmentation algorithms and have difficulty in segmenting deformable organs.

Figure 3 illustrates a flowchart of our method of segmenting the bony structures that will later guide the prostate and rectum segmentation. For each input image, we perform a pre-processing step that contains a median filter to remove noise, a 3-cluster k-means algorithm and morphological open, close, and fill operations to fill in the bone regions. We use 3 clusters since there are three main intensity bands of interest at this stage: bones with bright intensities, muscles and tissues with roughly gray intensities, and air and background with dark intensities. The images are processed slice by slice from the bottom to the top. The first slice typically contains only femurs. We use a standard roundness measure, i.e., $Roundness = 4\pi * area/perimeter^2$ to detect the left and right femurs. We then use a simple slice tracking method discussed below to propagate the segmented information from the current slice to the next slice. We ultimately
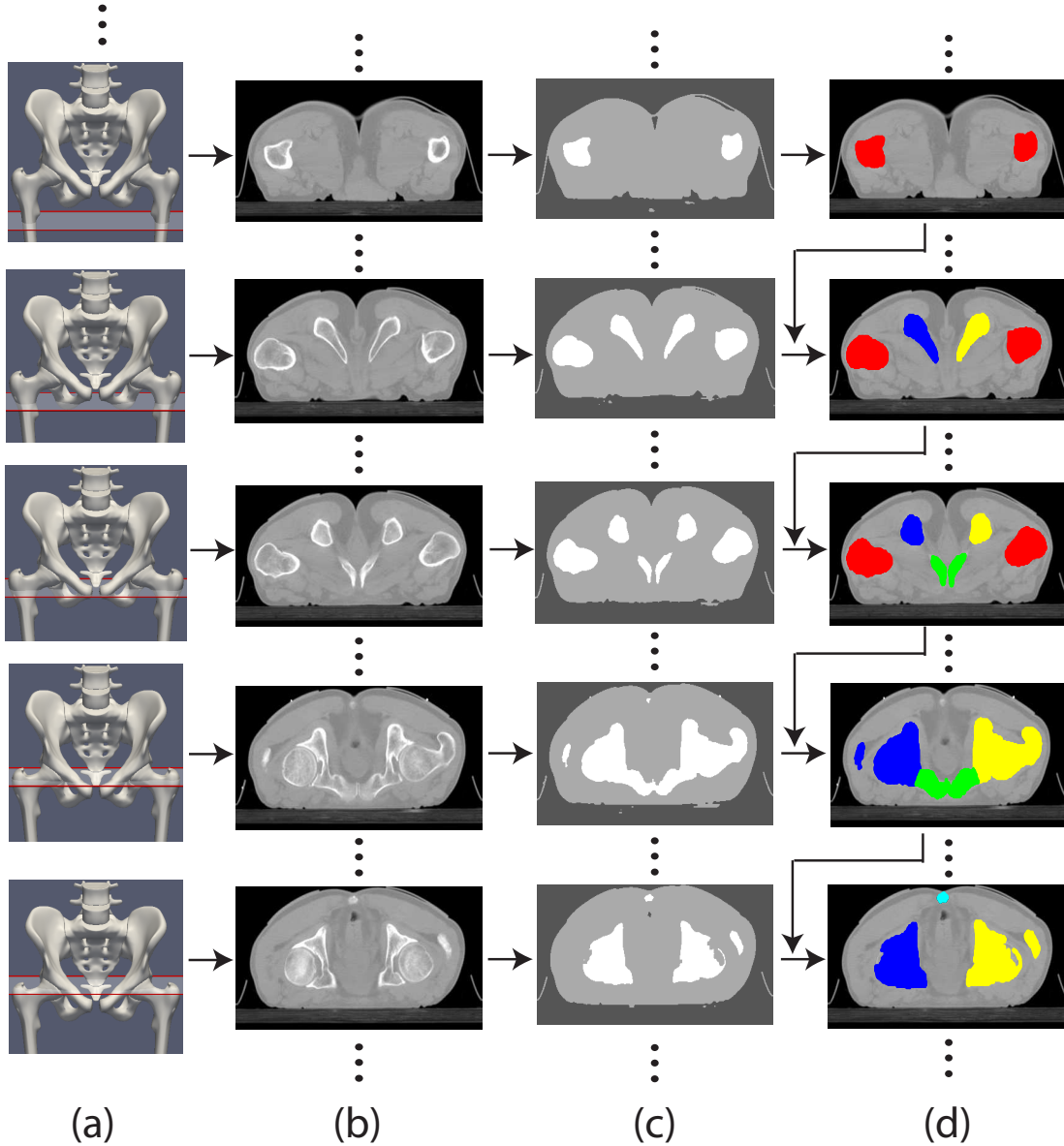
Fig. 3. Anatomy segmentation flowchart. (a) the slice location, (b) the slice image, (c) the k-means image after pre-processing, (d) the segmented bones: femurs in red, left pelvis in blue, right pelvis in yellow, front pelvis in green and coccyx in cyan. The figures in this paper are best viewed in color.

segment the front, left and right pelvic bones and coccyx based on this slice tracking algorithm.

The core of our bone segmentation algorithm is the propagation of the segmented organs from the previous slice to guide the segmentation of the current slice. Since the slices are usually sampled densely in the z direction, the spatial position of a bone changes little from slice to slice. This implies that the overlap of one bone on two consecutive slices is usually

quite significant and we can match the bones on the current slice based on their overlap with the already segmented bones of the previous slice. For relatively simple situations like Figure 4(a) and Figure 4(f), this simple heuristic works very well. However, when a merge or split occurs, we need to apply anatomical knowledge to identify different bone structures. When the left and right pelvic bones appear (Figure 4(b)), we can identify them based on their distance to the left/right femurs. When the left/right pelvic bones split (Figure 4(c)), we tag the lower bones as the front pelvis. When the femurs become attached to the left/right pelvic bones, (Figure 4(d)), they take on the latter label. Note that the coccyx is detected when a relatively large bone appears above the center of the mass of all the detected bones. Special care should be taken when the front pelvic bone is connected to the left and right pelvic bones as in Figure 4(e). We first search for the closest points between the left/front and right/front pelvic bones from the previous slice, and connect these with a line (red dots/lines in Figure 4(e)). If the coccyx doesn't exist on this slice, we simply estimate the coccyx position by raising the center of the mass by 50 pixels (black dot in Figure 4(e)). Then we draw a line connecting the coccyx (or the estimated coccyx) through the bisecting points of the red lines and split the bones respectively (Figure 4(e) bottom).

Once the bony structures are identified on each slice, we segment the inner boundaries of the pelvic and coccyx bones in order to form the anatomical constraints. To segment the inner boundaries of the pelvic bones, we extend rays from the coccyx to all the pelvic bone boundary points. As mentioned above, we estimate the coccyx position by raising the center of mass (magenta points in Figure 5) by 50 pixels if the coccyx doesn't exist in a given slice. If a given ray doesn't intersect with any other bone pixel, the corresponding bone boundary point is considered as an inner boundary point. The inner boundaries need not be connected. To segment the inner boundary of the coccyx, we apply the same procedure by extending rays from the center of the mass to the coccyx boundary points. The results are illustrated in Figure 5.

Next, we fit four 3D planes through all inner bone boundary points detected on the left/right/front pelvic bones and coccyx respectively. This plane fitting is accomplished in the usual way by minimizing the distances from the points to the plane, i.e., the mean square error fitting method. Figure 6(a) shows a 3D view of the pelvic bony structure with different colors illustrating the different automatically classified bones. Figure 6(b) and (c) illustrate different views of the 3D planes fit to the inner bone boundary points, indicating how they constrain the prostate and the
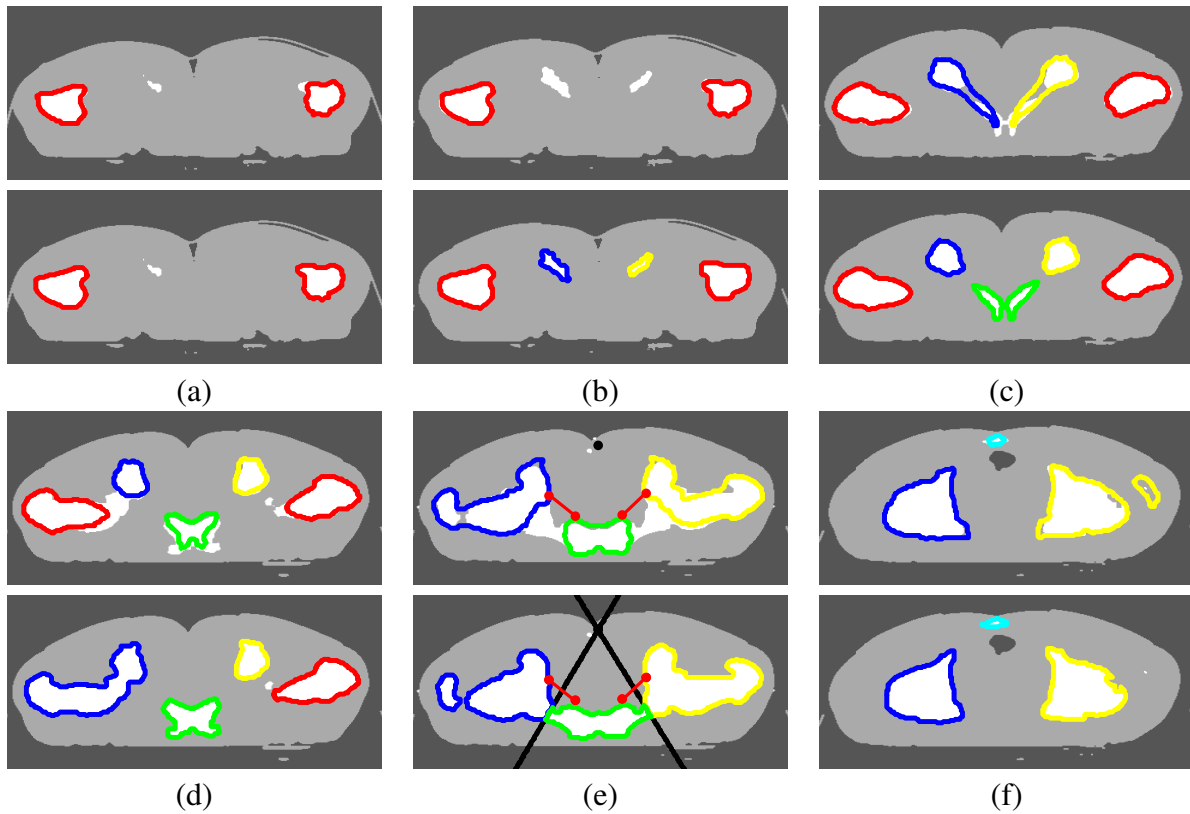
Fig. 4. Slice tracking examples. The k-means image after pre-processing of a given slice is displayed in both the top and bottom of each subfigure. The outer boundaries of bones from the previous slice are superimposed on the top subimage while the boundaries estimated for the current slice are superimposed on the bottom subimage. The red contours are the boundaries of the femurs. The blue contour is the boundary of the left pelvis. The yellow contour is the boundary of the right pelvis. The green contour is the boundary of the front pelvis. The cyan contour is the boundary of the coccyx. (a) femurs only, (b) pelvic bones appear, (c) pelvic bones split, (d) femurs attach to the pelvic bones, (e) front pelvic bones connect to the left/right pelvic bones, (f) coccyx and left/right pelvic bones only.
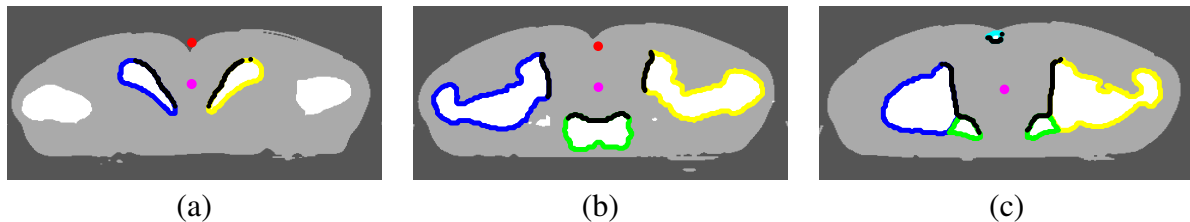

Fig. 5. Inner bone boundary segmentation examples. The k-means image after pre-processing is displayed. The red points are the estimated coccyx position. The magenta points are the center of mass on each slice. The black contours are the estimated inner bone boundaries.

rectum. As discussed below, we propose to incorporate the distances of the prostate and rectum to these four planes into the segmentation cost function as an "anatomy cost".
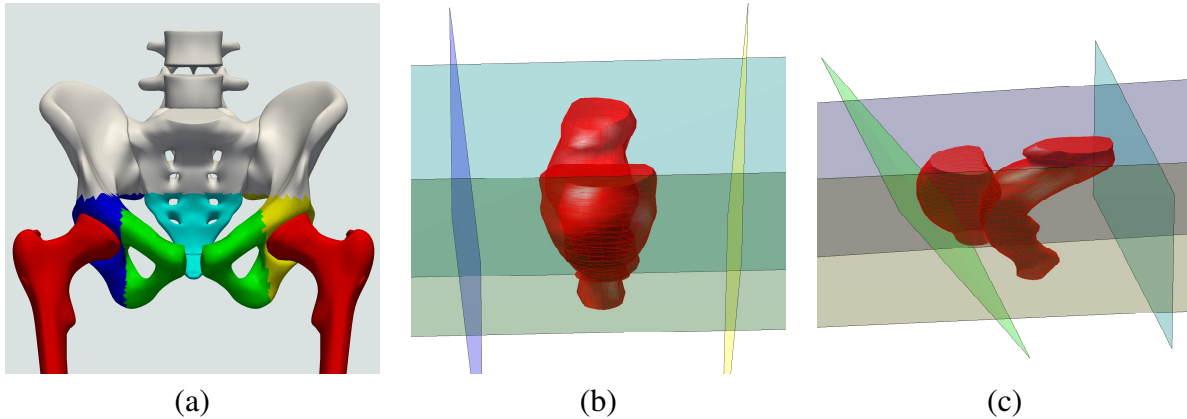
Fig. 6. 3D illustration of the anatomy segmentation. (a) illustration of different bony structures classified automatically (color code is the same as in Figure 4, (b),(c) different views of 3D planes built from inner bone boundary points. The colors of the planes in (b) and (c) match the colors of the different bone structures in (a).

IV. PARAMETRIC SHAPE MODEL

The first step of our model-based segmentation is to build a shape model. In this paper, we used the original ASM introduced by Cootes et al. [9] because of its simplicity and well-studied behavior. However, our segmentation framework can be easily applied to other shape models. As noted in Section II , before PCA can be applied, the correspondence between landmark points of training shapes must be calculated. We adopt the method introduced by Jeong and Radke [25] for efficient resampling of contours that gives reasonable pixel correspondence, briefly described below.

Our training data consists of 3D pelvic CT data sets each composed of 20–40 axial slices, each slice with 10–30 marker points manually placed by a physician to outline the organs of interest (i.e., the prostate and rectum). No registration of scans from different patients is required, since the coordinate system is described with respect to the isocenter designated by the physician for the radiotherapy application. The main idea of the resampling work introduced in [25] is to resample each training dataset into the same number of slices by interpolating Elliptic Fourier Descriptor (EFD) coefficients. The building block is that each closed planar curve $x(t), y(t), t \in (0, 2\pi)$ can be uniquely expressed as a weighted sum of the Fourier coefficients:

$$
\begin{bmatrix} x(t) \\ y(t) \end{bmatrix} = \begin{bmatrix} a_0 \\ c_0 \end{bmatrix} + \sum_{k=1}^{\infty} \begin{bmatrix} a_k & b_k \\ c_k & d_k \end{bmatrix} \begin{bmatrix} \cos kt \\ \sin kt \end{bmatrix}
\tag{1}
$$

where the coefficients $[a_0, c_0, a_1, b_1, c_1, d_1]$ are given by:

$$
\begin{aligned}
a_0 &= \frac{1}{2\pi} \int_0^{2\pi} x(t) \; dt & c_0 &= \frac{1}{2\pi} \int_0^{2\pi} y(t) \; dt \\
a_k &= \frac{1}{\pi} \int_0^{2\pi} x(t) \cos kt \; dt & b_k &= \frac{1}{\pi} \int_0^{2\pi} x(t) \sin kt \; dt \\
c_k &= \frac{1}{\pi} \int_0^{2\pi} y(t) \cos kt \; dt & d_k &= \frac{1}{\pi} \int_0^{2\pi} y(t) \sin kt \; dt
\end{aligned}
\tag{2}
$$

First, we interpolate the original points on each slice with cubic splines to obtain finely sampled $x(t), y(t)$ curves for each slice (Figure 7(a),(b)). We then calculate the EFD coefficients of the original slices using a discretized version of (2), using the same number of EFD coefficients for each slice. The higher the number of EFD coefficients, the higher the spatial frequency can be captured; in this work we choose $k = 6$. A slice with height z_i is thus represented by a vector of EFD coefficients $[a_0(z_i), c_0(z_i), a_1(z_i), b_1(z_i), c_1(z_i), d_1(z_i), \ldots, d_k(z_i)]$. Then we interpolate and evaluate these vectors at uniformly sampled locations $z_j, j = 1, ..., N$ where N is a user defined number of slices (in this paper, $N = 20$). The resampled contour at height z_j is then reconstructed according to (1) from $[a_0(z_j), c_0(z_j), a_1(z_j), b_1(z_j), c_1(z_j), d_1(z_j), \ldots, d_k(z_j),]$ (Figure 7c). After establishing the axial correspondence across training shapes according to this resampling procedure, we can obtain the point correspondence at consistent locations on each 2D slice based on arc-length and angle constraints. We do this by extending M rays from the slice's center of gravity at uniform angles at $\theta_m = \frac{2\pi m}{M}, m = 0, \ldots, M-1$, to the slice boundary (Figure 7d). This will result in consistent selection of corresponding landmarks because in CT applications, the patients are always imaged in the same orientation with respect to the treatment couch and the organs from different scans are already aligned with respect to rotation. In this work, we choose $M = 20$; that is each shape is resampled into 20 slices with 20 points each. For a complete discussion of the resampling procedure, we refer the readers to the original article [25].

After resampling, each training shape is represented by a 400 by 3 matrix, or a vector of dimension 1200 by stacking the x, y and z coordinates. For joint prostate and rectum segmentation, we stack the prostate and rectum points for each patient into a vector of dimension 2400. Given n training sets, we perform PCA on this 2400 by n matrix. The mean shape $\bar{S}$ and orthogonal eigenvectors P resulting from PCA are used as the shape model to produce a new
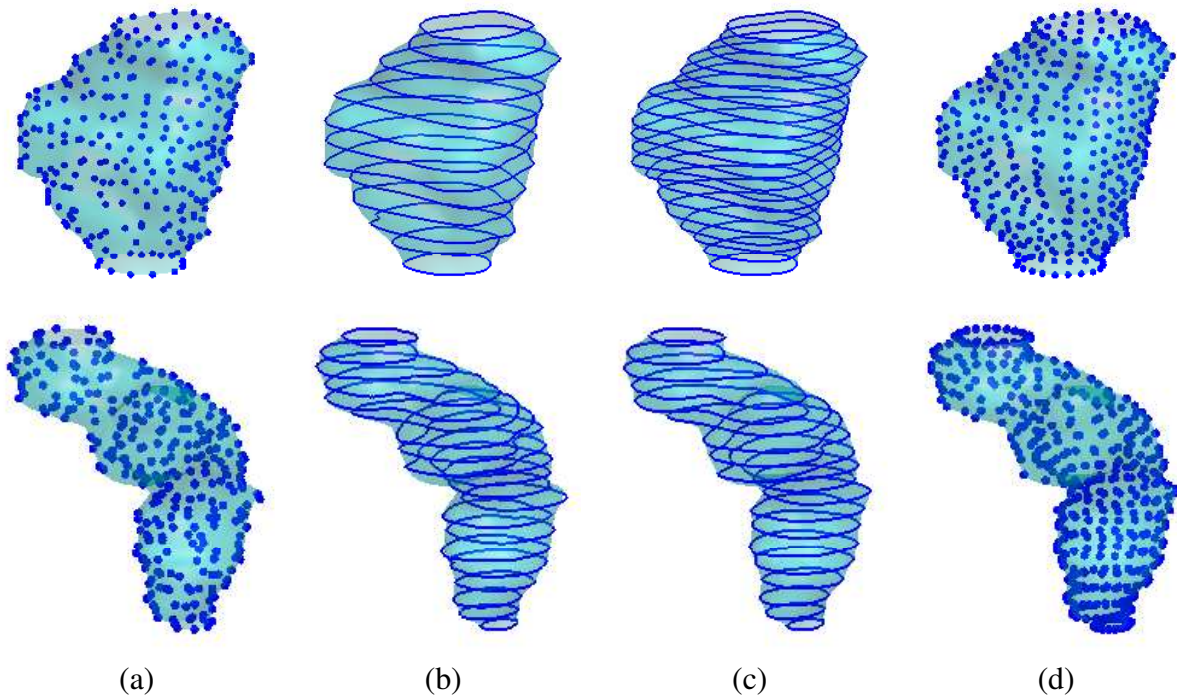
Fig. 7. Resampling procedure for the prostate (top row) and the rectum (bottom row). (a) original landmarks placed by physicians, (b) original slices interpolated from landmarks, (c) interpolated slices using EFD method, (d) corresponding landmarks placed along interpolated slices using ray extension method.

shape S^β:

$$S^\beta = \bar{S} + P\beta \tag{3}$$

in which different β parameters produce different shapes. Therefore, the segmentation problem is equivalent to finding the best β for a given 3D CT dataset.

One problem here is the dimension of β. Recent work [33] shows that the optimum PCA dimension is a trade-off between the ability to model the structure variation and the noise. With more modes, we have a more accurate shape reconstruction. However, more modes will not only increase the risk of overfitting [33], complicating the search for the best β, but also will make estimating $p(\beta|\tilde{\beta})$ more difficult. Silverman [41] pointed out that with increasing dimensionality, the number of samples required in kernel density estimation increases quickly. In our work, we adopt the traditional approach, choosing the number of modes that reflect 95% of the shape variation in the training dataset. For our data, this results in 8 modes.

V. SEGMENTATION ALGORITHM

A. *Segmentation using Bayesian Inference*

In a Bayesian framework, the problem of segmentation is to find the most likely $\hat{\beta}$ based on all the information from the training images and the target image.

$$
\begin{aligned}
\hat{\beta} &= \arg\max p(\beta | training, target) \\
&\propto \arg\max p(target | \beta, training) \cdot p(\beta | training) \quad (4)
\end{aligned}
$$

where $p(target | \beta, training)$ is the likelihood of observing the target image if we are given the organs' locations, and $p(\beta | training)$ is the prior probability of the organs' locations, which only depends on the training shapes.

The target image contains both *intensity information* and *anatomy information*. We characterize the *intensity information* corresponding to a given β using the histograms of pixel intensities inside each organ (h_{in}), outside the organs (h_{out}), and inside the entire domain (h_{en}), extracted as described below. Computed histograms learned from the training data are represented by $\tilde{h}_{in}$, $\tilde{h}_{out}$, and $\tilde{h}_{en}$. We denote the *anatomy information* for the target image as γ and for the training images as $\tilde{\gamma}$, as described below. We define the best-fit parameters of the training shapes as $\tilde{\beta}$, computed from projecting the ground-truth contours onto the shape model. Using this notation, (4) can be further decomposed as:

$$
\begin{aligned}
&p(target | \beta, training) \cdot p(\beta | training) \\
&\propto \ p\Big(h_{in}(\beta), h_{out}(\beta), h_{en}(\beta), \gamma(\beta) | training\Big) \cdot p(\beta | \tilde{\beta}) \\
&\propto \ p\Big(h_{in}(\beta), h_{out}(\beta), h_{en}(\beta) | training\Big) \cdot p\Big(\gamma(\beta) | training\Big) \cdot p(\beta | \tilde{\beta}) \\
&\propto \ {\color{red} p\Big(h_{in}(\beta), h_{out}(\beta), h_{en}(\beta) | \tilde{h}_{in}, \tilde{h}_{out}, \tilde{h}_{en}\Big)} \cdot {\color{green} p\Big(\gamma(\beta) | \tilde{\gamma}\Big)} \cdot {\color{blue} p(\beta | \tilde{\beta})} \quad (5)
\end{aligned}
$$

Thus, the segmentation cost function separates into three parts. The red term in (5) is an intensity cost that measures the likelihood of observing the intensity information. The green term is an anatomy cost that measures the likelihood of observing the anatomy information.

The blue term is a shape cost that measures the prior probability of observing the shape.[1] We explicitly define these expressions as follows.

1) Intensity cost: In our method, we simply choose the region exterior to the organ and interior to the patient body as the "outside". In our previous work [14], the intensity cost was defined as the cumulative-density-function distance between the interior histogram of the target model's current position in the image and a reference histogram learned from training data. The accuracy of the reference histogram determined the success of segmentation. Here, we bypass the sensitive step of estimating the unknown reference histogram by incorporating all training histograms in a probabilistic approach, initially proposed by us in [5]. Three key things to notice are that: 1) h_{in} and h_{out} are functions of β, 2) h_{en} is independent of β, and 3) there is a simple relation between h_{in}, h_{out}, and h_{en}:

$$h_{en} = \alpha h_{in} + (1 - \alpha) h_{out} \tag{6}$$

where $\alpha = volume_{inside} / volume_{entire}$, and $volume$ denotes the number of pixels in each region.

These allow us to decompose the image energy term as follows:

$$
\begin{aligned}
& p\left(h_{in}(\beta), h_{out}(\beta), h_{en} | \tilde{h}_{in}, \tilde{h}_{out}, \tilde{h}_{en}\right) \\
\propto \quad & p\left(h_{en} | h_{in}(\beta), h_{out}(\beta), \tilde{h}_{in}, \tilde{h}_{out}, \tilde{h}_{en}\right) \times p\left(h_{in}(\beta), h_{out}(\beta) | \tilde{h}_{in}, \tilde{h}_{out}, \tilde{h}_{en}\right) \\
=^1 \quad & \int p\left(h_{en}, \alpha | h_{in}(\beta), h_{out}(\beta), \tilde{h}_{in}, \tilde{h}_{out}, \tilde{h}_{en}\right) d\alpha \times p\left(h_{in}(\beta) | \tilde{h}_{in}\right) \times p\left(h_{out}(\beta) | \tilde{h}_{out}\right) \\
=^2 \quad & \int p\left(h_{en} | h_{in}(\beta), h_{out}(\beta), \alpha\right) p\left(\alpha | \tilde{h}_{in}, \tilde{h}_{out}, \tilde{h}_{en}\right) d\alpha \times p\left(h_{in}(\beta) | \tilde{h}_{in}\right) \times p\left(h_{out}(\beta) | \tilde{h}_{out}\right) \\
=^3 \quad & \int \delta\left(\alpha - \alpha(\beta)\right) p\left(\alpha | \tilde{\alpha}\right) d\alpha \times p\left(h_{in}(\beta) | \tilde{h}_{in}\right) \times p\left(h_{out}(\beta) | \tilde{h}_{out}\right) \\
= \quad & p\left(\alpha(\beta) | \tilde{\alpha}\right) \times p\left(h_{in}(\beta) | \tilde{h}_{in}\right) \times p\left(h_{out}(\beta) | \tilde{h}_{out}\right) \tag{7}
\end{aligned}
$$

Equality 1 holds because we assume that h_{in} and h_{out} are independent. Equality 2 holds because h_{en} is conditionally independent with the training images given h_{in}, h_{out} and α. Similarly, α is independent of h_{in} and h_{out} when h_{en} is unknown. Equality 3 holds because of (6), where δ is the Kronecker delta function.

---

[1] We note that while the anatomy information (i.e., bone locations) is originally estimated based on image information and is thus not truly independent from it, for the purposes of segmentation we treat the anatomy structures as pre-defined information, independent from the image intensities.

Thus, the intensity cost can finally be written as:

$$p\big(\alpha(\beta)|\tilde{\alpha}\big) \cdot p\big(h_{prostate}(\beta)|\tilde{h}_{prostate}\big) \cdot p\big(h_{rectum}(\beta)|\tilde{h}_{rectum}\big) \cdot p\big(h_{out}(\beta)|\tilde{h}_{out}\big) \tag{8}$$

where $\alpha(\beta) = [\alpha_{prostate}(\beta) \quad \alpha_{rectum}(\beta)]^T = [vol_{prostate}(\beta)/vol_{entire} \quad vol_{rectum}(\beta)/vol_{entire}]^T$.

We model $p\big(\alpha(\beta)|\tilde{\alpha}\big)$ as a 2-dimensional Gaussian distribution with mean μ_α and covariance Σ_α estimated from the training data:

$$p\big(\alpha(\beta)|\tilde{\alpha}\big) = \frac{1}{2\pi|\Sigma_\alpha|^{1/2}} \exp\left[-\frac{1}{2}(\alpha(\beta) - \mu_\alpha)^T \Sigma_\alpha^{-1}(\alpha(\beta) - \mu_\alpha)\right] \tag{9}$$

The densities $p\big(h_{prostate}(\beta)|\tilde{h}_{prostate}\big)$, $p\big(h_{rectum}(\beta)|\tilde{h}_{rectum}\big)$, and $p\big(h_{out}(\beta)|\tilde{h}_{out}\big)$ are distributions over histograms and we adopt the idea of kernel density estimation to define them:

$$p(h|\tilde{h}) \propto \frac{1}{N} \sum_{i=1}^{N} \exp\left(-\frac{1}{2\sigma_h^2} D(h, \tilde{h}_i)\right) \tag{10}$$

where N is the number of training histograms, σ_h is a kernel width, and $D(h, \tilde{h}_i)$ is defined as

$$D(h, \tilde{h}_i) = \sum_{j=1}^{n} |p_j - q_j| \tag{11}$$

where p_j, q_j are the n-bin cumulative distribution functions of h and $\tilde{h}_i$ [14].

2) Shape cost: ASM [9] and HPDM [21] addressed the problem of specifying a valid shape region (i.e., an allowable set of β) by hard-constraining the search of shape parameters to a region where the resulting shape is similar to the training shapes. These approaches suffer from the difficulties that either the valid shape region is too loose to define meaningful valid shapes or too tight that other valid shapes may be excluded from the region. We adopt the idea introduced by Cremers et al. [11] of forming a kernel density shape prior distribution that encodes valid shape region information into the cost function.

From our shape model (3), we know that a shape is specified by a set of parameters β, so the shape prior can be effectively turned into a parameter prior. Given a set of training shapes $\{\tilde{\beta}_i\}_{i=1...N}$, we define a probability prior density on the parameters using a kernel density estimator:

$$p(\beta \mid \tilde{\beta}) \propto \frac{1}{N} \sum_{i=1}^{N} \exp\left(-\frac{1}{2\sigma_\beta^2} ||\beta - \tilde{\beta}_i||^2\right) \tag{12}$$

3) Anatomy cost: In Section III, we described our approach of segmenting the bone structures to form anatomy constraints. We use the minimum Euclidean distances from the prostate surface to the 3 bone planes and the minimum distance from the rectum surface to the coccyx plane to quantify these soft constraints. We use this 4-dimensional vector $\gamma = [d_1, \ldots, d_4]$ to represent the anatomical likelihood of the location of the prostate and rectum given their proximity to the bones. Similar to the other costs, $p(\gamma|\tilde{\gamma})$ is defined using a kernel density estimator:

$$p(\gamma|\tilde{\gamma}) \propto \frac{1}{N} \sum_{i=1}^{N} \exp\left(-\frac{1}{2\sigma_\gamma^2}||\gamma - \tilde{\gamma}_i||^2\right) \tag{13}$$

The accurate calculation of the minimum distance from an arbitrary 3D object to a plane is time-consuming. However, due to our point-based shape representation, we can approximate this distance by the minimum distance from the point set to the plane, which can be computed quickly.

4) Segmentation cost function: Combining all three component cost functions, maximizing (5) is equivalent to minimizing:

$$- log(p(h_{prostate}|\tilde{h}_{prostate})) - log(p(h_{rectum}|\tilde{h}_{rectum})) - log(p(h_{out}|\tilde{h}_{out}))$$

$$- log(p(\alpha|\tilde{\alpha})) - log(p(\beta|\tilde{\beta})) - log(p(\gamma|\tilde{\gamma})) \tag{14}$$

The main issue is defining the widths σ in each kernel density estimator. We followed the approach proposed by Silverman [41], in which σ is defined as the median inter-training-sample distance. This will give neither a too narrow nor a too broad kernel width.

VI. SEGMENTATION RESULTS

We now apply the model-based segmentation technique to the fully automatic segmentation of the prostate and rectum from 3D CT imagery. For the optimization, we used the Broyden-Fletcher-Goldfarb-Shanno (BFGS) method with inverse Hessian updates [36]. Due to the difficulty of obtaining the analytic gradient of the entire cost function, we use a numerical gradient. In our experiments with unoptimized Matlab code on an Intel Core 2 CPU, 3.5GB RAM computer, our algorithm typically runs in less than 1 minute for joint prostate and rectum segmentation, compared to the 15-20 minutes it may take a physician to perform the same task.

Our training data comes from a 13-patient study in which each patient dataset contains 11 to

17 full 3D scans taken on different days of treatment, totalling 185 scans. The experiment is done with a leave-one-out method where all the datasets from one patient were excluded from the training sets. For example, if we want to segment the prostate and rectum of patient 1, we train the model with the rest of the datasets from all the other patients and segment the datasets of patient 1 by applying the prostate-rectum joint model described in Section V. The statistical segmentation results are then compared with the contours drawn by a physician, considered to be the ground truth for the purposes of this study.
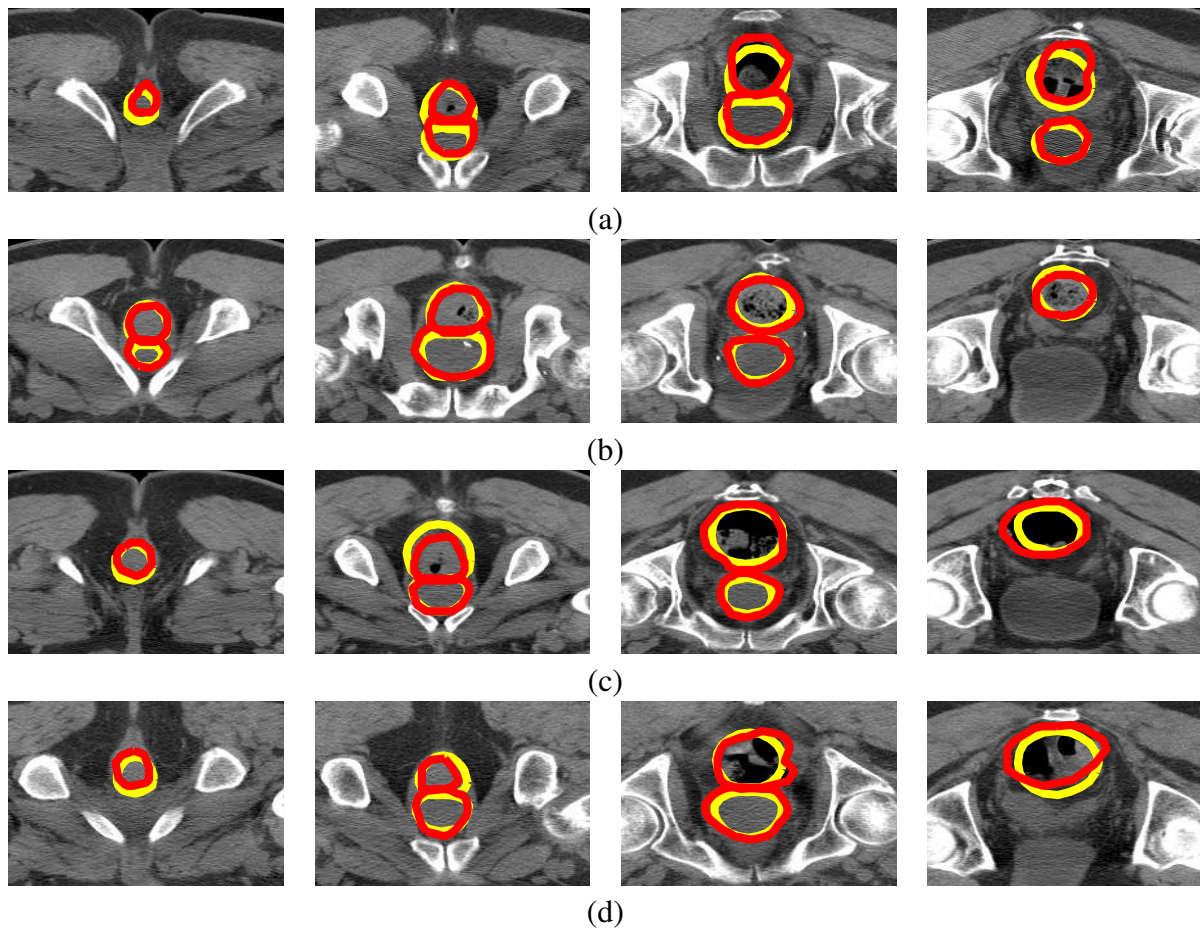

Fig. 8. Sample automatic segmentation results of the prostate and rectum. The yellow contours are ground truth outlined by a physician and the red contours are automatic segmentation results. (a) patient 3, (b) patient 5, (c) patient 7, (d) patient 8.

We initialize the segmentation process at the mean shape of the PCA model. We found that due to the anatomy cost component, our algorithm is relatively robust to initialization. Figure 8 shows the automatic segmentation results for four 2D axial images from four different patients (note that the segmentation algorithm is fully 3D). The red contours are manually outlined by

a physician from our collaborator hospital Memorial Sloan-Kettering Cancer Center (MSKCC). The yellow contours are automatic segmentation results using our algorithm. Figure 9 shows the 3D visualization of the final prostate-rectum segmentation results of 12 test scans from 12 different patients.
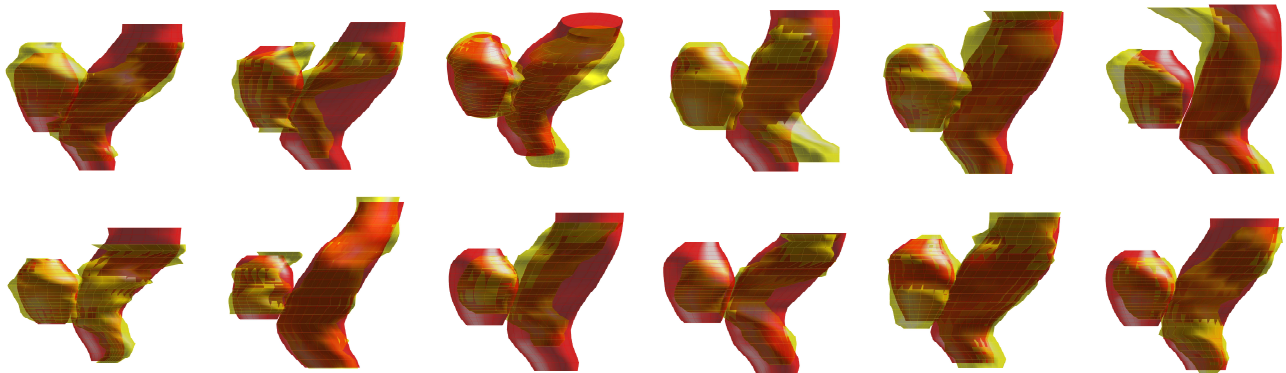

Fig. 9.   3D visualizations of segmentation results for 12 different patients. The yellow surfaces are the ground truth and the red surfaces are the automatic segmentation results. First row, from left to right: patient 1–6. Second row, from left to right:patient 7–12

We also calculated several quantitative measurements of the segmentation results over the 185 datasets in Table I, following the approach in [14].

- v_d, the probability of detection, i.e., the percentage of the ground truth volume overlapping the automatic segmentation result. For a good segmentation, v_d should be close to 1.
- v_{fa}, the probability of false alarm, i.e., the percentage of the segmentation result volume that lies outside the ground truth. For a good segmentation, v_{fa} should be close to 0.
- The surface distance d_s, calculated as the maximum distance between the surfaces of the ground truth and segmented organs. The distance was computed over 1000 rays originating from the ground truth centroid and cast outwards using a uniform spherical distribution.

We also compared results obtained using different cost functions in Table II. The cost functions evaluated included:

- The full cost function (5)
- (5) without the anatomy cost (green term)
- (5) without the shape cost (blue term)
- our previous cost function in [14].

Table I and II tell us that:

patient ID	1	2	3	4	5	6	7	8	9	10	11	12	13
median v_d, prostate	0.70	0.80	0.90	0.69	0.83	0.63	0.87	0.78	0.77	0.98	0.95	0.97	0.94
median v_d, rectum	0.80	0.70	0.85	0.67	0.86	0.72	0.75	0.66	0.85	0.73	0.68	0.77	0.78
median v_{fa}, prostate	0.17	0.33	0.08	0.26	0.07	0.19	0.10	0.05	0.14	0.34	0.14	0.34	0.24
median v_{fa}, rectum	0.28	0.23	0.18	0.31	0.12	0.28	0.06	0.15	0.34	0.36	0.37	0.24	0.12
mean d_s, prostate (mm)	1.8	1.4	0.8	2.2	0.6	2.1	0.6	0.6	1.5	1.4	1.8	0.6	1.0
mean d_s, rectum (mm)	2.4	3.6	2.4	3.1	1.0	2.5	1.8	2.6	2.4	3.4	2.4	2.5	1.3
median d_s, prostate (mm)	1.7	1.5	0.9	2.3	0.6	2.0	0.8	0.7	1.3	1.3	1.8	0.7	1.1
median d_s, rectum (mm)	2.3	3.3	2.1	3.3	1.4	2.7	1.7	2.6	2.4	3.3	2.4	2.6	1.3
max d_s, prostate (mm)	3.1	3.7	2.6	4.9	2.0	4.3	2.8	2.7	3.2	3.7	3.9	2.7	3.0
max d_s, rectum (mm)	4.7	4.9	4.2	5.1	3.0	4.4	4.5	5.7	4.4	4.9	5.1	4.8	3.7

TABLE I

QUANTITATIVE MEASURES OF SEGMENTATION RESULTS OVER 185 TESTING SCANS USING OUR ALGORITHM.

	Our algorithm		without anatomy cost		without shape cost		previous cost [14]	
Quantitative measure	prostate	rectum	prostate	rectum	prostate	rectum	prostate	rectum
median v_d	0.84	0.71	0.61	0.60	0.73	0.64	0.62	0.63
median v_{fa}	0.13	0.24	0.26	0.38	0.22	0.35	0.36	0.48
median surface distance (mm)	1.1	2.2	1.3	2.6	1.6	2.7	2.0	2.7

TABLE II

QUANTITATIVE MEASURES OF SEGMENTATION RESULTS OVER 185 TESTING SCANS BY COMPARING OUR COST FUNCTIONS
WITH OTHER COST FUNCTIONS.

- The shape and anatomical costs improve all measures of performance, enabling prostate segmentation accuracy of roughly 1.1mm and rectum segmentation accuracy of roughly 2.2mm.

- Comparing the results without the anatomy cost and the results without the shape cost, we see that the anatomy cost plays a more important role. This also makes sense because anatomy information is more physically meaningful and a harder constraint compared with shape information.

- We noticed that physicians sometimes ignore the top- and bottom-most slices of the prostate and rectum when contouring, which can lead to artificially large v_{fa} values.

- Based on Figure 9 and Table I, we noticed that the rectum segmentation may be suboptimal for some patients (e.g., patients 4 and 6) due to uncommon shape variation at either end of the rectum. Incorporating additional training sets or a more advanced shape modeling

technique may address this issue.

To illustrate the importance of incorporating anatomy information, Figure 10 compares axial slices for one patient with and without the anatomy cost (green term) in the cost function (5). We can observe marked improvement when using the constraints.
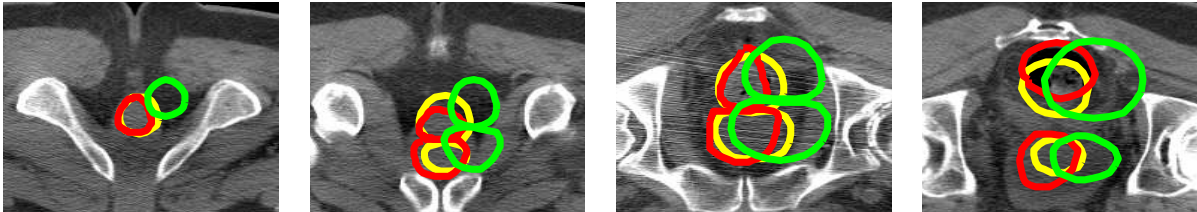

Fig. 10. Four axial slices of automatic segmentation results for one patient, illustrating the importance of incorporating anatomy information. The yellow contours are ground truth outlined by a physician, the red contours are segmentation results with the anatomy cost and the green contours are the segmentation results without the anatomy cost.

VII. CONCLUSIONS AND FUTURE WORK

We proposed a new segmentation cost function incorporating learned intensity, shape and anatomy information from training images and presented automatic segmentation results on the prostate and rectum. We believe that incorporating all three pieces of information is a promising direction for solving difficult medical image segmentation problems.

The segmentation framework is derived using Bayesian inference, so it is easy to adapt to other non-medical segmentation tasks by considering only intensity and shape cost. In addition, we found the framework to be robust to noise and initialization, and flexible in terms of its modeling and segmenting ability.

While the segmentation performance of the algorithm was generally encouraging, we did notice a few segmentation failures- most often in cases where the ground-truth organ contours were highly atypical in shape, position, or intensity distribution. Such cases are easily detectable from high values of the cost function and can be used to cue manual contouring. We also noticed that when the intensity distribution between the prostate and bladder is indistinguishable, the algorithm sometimes includes some bladder regions in the prostate segmentation.

One goal for future research is to incorporate the bladder into the joint model, both to avoid the problem above and to improve the clinical usefulness of the algorithm. Due to the special anatomical structure of the pelvic organs, the shape and location of the bladder has a great

influence on the prostate. However, unlike the prostate and rectum that have relatively fixed shapes, the bladder can deform and change volume in an unpredictable manner, and a linear model may not be able to capture this shape variation. We are currently investigating KPCA to represent the nonlinear shape variation, but the "pre-image" problem is difficult to solve.

We are also investigating substitutions for the histograms in the intensity cost function. Since histograms totally discard spatial information, they may be suboptimal for the rectum, in which the intensity distribution has a characteristic pattern.

The performance of our segmentation results also depends on the accuracy of the estimate of the anatomy information. Our current approach to segment the bones and muscles may not be robust (for example) to cases where clips or markers have been inserted into the prostate. As needed, we will investigate more robust bony-pelvis registration-based segmentation algorithms for the anatomy definition step.

ACKNOWLEDGMENTS

REFERENCES

[1] R. Bansal, L. H. Staib, Z. Chen, A. Rangarajan, J. Knisely, R. Nath, and J. S. Duncan. Entropy-based dual-portal-to-3D-CT registration incorporating pixel correlation. *IEEE Transactions on Medical Imaging*, 22(1), 2003.

[2] M. Brejl and M. Sonka. Object localization and border detection criteria design inedge-based image segmentation: automated learning from examples. *IEEE Transactions on Medical Imaging*, 19(10):973–985, 2000.

[3] R. E. Broadhurst, J. Stough, S. M. Pizer, and E. L. Chaney. Histogram statistics of local model-relative image regions. In *Deep Structure, Singularities, and Computer Vision*, 2005.

[4] T. Chan and L. Vese. Active contours without edges. *IEEE Transactions on Image Processing*, 10(2), 2001.

[5] S. Chen and R. J. Radke. Level set segmentation with both shape and intensity priors. In *Proceedings of IEEE International Conference on Computer Vision*, 2009.

[6] H. Chui, A. Rangarajan, J. Zhang, and C. M. Leonard. Unsupervised learning of an atlas from unlabeled point-sets. *IEEE Transactions on Pattern Analysis and Machine Intelligence*, 26(2), 2004.

[7] D. C. Collier, S. S. C. Burnett, M. Amin, S. Bilton, et al. Assessment of consistency in contouring of normal-tissue anatomic structures. *Journal of Applied Clinical Medical Physics*, 4(1), 2003.

[8] T. F. Cootes, G. J. Edwards, and C. J. Taylor. Active appearance models. *IEEE Transactions on Pattern Analysis and Machine Intelligence*, 23(6):681–685, 2001.

[9] T. F. Cootes, C. J. Taylor, D. H. Cooper, and J. Graham. Active shape models-their training and application. *Computer Vision and Image Understanding*, 61(1):38–59, 1995.

[10] M. Costa, H. Delingette, S. Novellas, and N. Ayache. Automatic segmentation of bladder and prostate using coupled 3D deformable models. In *International Conference on Medical Image Computing and Computer-Assisted Intervention*, 2007.

[11] D. Cremers, S. J. Osher, and S. Soatto. Kernel density estimation and intrinsic alignment for shape priors in level sets segmentation. *International Journal of Computer Vision*, 69(3), 2006.

[12] R. H. Davies, C. J. Twining, T. F. Cootes, and C. J. Taylor. A minimum description length approach to statistical shape modeling. *IEEE Transactions on Medical Imaging*, 21(5), 2002.

[13] M. Foskey, B. Davis, L. Goyal, S. Chang, E. Chaney, N. Strehl, S. Tomei, J. Rosenman, and S. Joshi. Large deformation three-dimensional image registration in image-guided radiation therapy. *Physics in Medicine and Biology*, 50, 2005.

[14] D. Freedman, R. J. Radke, T. Zhang, Y. Jeong, D. M. Lovelock, and G. T. Y. Chen. Model-based segmentation of medical imagery by matching distributions. *IEEE Transactions on Medical Imaging*, 24(3), 2005.

[15] D. Freedman and T. Zhang. Interactive graph cut based segmentation with shape priors. In *Proceedings of the 2005 IEEE Computer Society Conference on Computer Vision and Pattern Recognition*, 2005.

[16] W. T. Freeman and J. B. Tenenbaum. Learning bilinear models for two-factor problems in vision. In *Proceedings of IEEE Conference on Computer Vision and Pattern Recognition*, 1997.

[17] P. Ghosh and M. Mitchell. Segmentation of medical images using a genetic algorithm. In *Proceedings of the 8th annual conference on Genetic and evolutionary computation*, 2006.

[18] F. Gibou, D. Levy, C. Cardenas, P. Liu, and A. Boyer. Partial differential equations-based segmentation for radiotherapy treatment planning. *Math. Biosci. Eng*, 2:209–226, 2005.

[19] H. Gray. *Anatomy of the human body*. Philadelphia : Lea and Febiger, 1918.

[20] B. Haas, T. Coradi, M. Scholz, P. Kunz, et al. Automatic segmentation of thoracic and pelvic CT images for radiotherapy planning using implicit anatomic knowledge and organ-specific segmentation strategies. *Physics in Medicine and Biology*, 53(6):1751–1772, 2008.

[21] T. Heap and D. Hogg. Improving specificity in PDMs using a hierachical approach. In *Proceedings of the 8th British Machine Vision Conference*, 1997.

[22] T. Heimann and H. Meinzer. Statistical shape models for 3D medical image segmentation: A review. *Medical Image Analysis*, 13(4):543–563, 2009.

[23] C. Hua, D. M. Lovelock, G. Mageras, M. Katz, et al. Development of a semi-automatic alignment tool for accelerated localization of the prostate. *International Journal of Radiation Oncology, Biology, Physics*, 55(3), 2003.

[24] Y. Jeong and R. J. Radke. Modeling inter- and intra-patient anatomical variation using a bilinear model. In *Proceedings of the IEEE Computer Society Workshop on Mathematical Methods in Biomedical Image Analysis*, 2006.

[25] Y. Jeong and R. J. Radke. Reslicing axially-sampled 3D shape using elliptic Fourier descriptors. *Medical Image Analysis*, 11(2), 2007.

[26] M. Kass, A. Witkin, and D. Terzopoulos. Snakes: Active contour models. *International Journal of Computer Vision*, 1(4):321–331, 1988.

[27] A. Kelemen, G. Szekely, and G. Gerig. Elastic model-based segmentation of 3D neuroradiological data sets. *IEEE Transactions on Medical Imaging*, 18(10), 1999.

[28] S. Klein, U. van der Heide, B. Raaymakers, A. Kotte, M. Staring, and J. Pluim. Segmentation of the prostate in MR images by atlas matching. In *4th IEEE International Symposium on Biomedical Imaging: From Nano to Macro*, 2007.

[29] M. E. Leventon, W. E. L. Grimson, and O. Faugeras. Statistical shape influence in geodesic active contours. In *Proceedings of IEEE Conference on Computer Vision and Pattern Recognition*, 2000.

[30] U. Malsch, C. Thieke, and R. Bendl. Fast elastic registration for adaptive radiotherapy. In *Proceedings of Medical Image Computing and Computer-Assisted Intervention*, 2006.

[31] S. Martin, V. Daanen, and J. Troccaz. Atlas-based prostate segmentation using an hybrid registration. *International Journal of Computer Assisted Radiology and Surgery*, 3(6):485–492, 2008.

[32] M. Mazonakis, J. Damilakis, H. Varveris, P. Prassopoulos, and N. Gourtsoyiannis. Image segmentation in treatment planning for prostate cancer using the region growing technique. *British Journal of Radiology*, 74, 2001.

[33] L. Mei, M. Figl, D. Rueckert, A. Darzi, and P. Edwards. Statistical shape modelling: How many modes should be retained? In *IEEE Computer Society Conference on Computer Vision and Pattern Recognition Workshops*, 2008.

[34] S. Mitchell, J. Bosch, B. Lelieveldt, R. Van der Geest, J. Reiber, and M. Sonka. 3-D active appearance models: segmentation of cardiac MR and ultrasound images. *IEEE Transactions on Medical Imaging*, 21(9):1167–1178, 2002.

[35] D. Nain, S. Haker, A. Bobick, and A. Tannenbaum. Multiscale 3-D shape representation and segmentation using spherical wavelets. *IEEE Transactions on Medical Imaging*, 26(4), 2007.

[36] J. Nocedal and S. J. Wright. *Numerical optimization*. Springer, 1999.

[37] S. Osher and J. Sethian. Fronts propagating with curvature-dependent speed- Algorithms based on Hamilton-Jacobi formulations. *Journal of Computational Physics*, 79:12–49, 1988.

[38] S. M. Pizer, D. S. Fritsch, P. A. Yushkevich, V. E. Johnson, and E. L. Chaney. Segmentation, registration and measurement of shape variation via image object shape. *IEEE Transactions on Medical Imaging*, 18(10), 1999.

[39] S. Romdhani, S. Gong, and A. Psarrou. A multi-view non-linear active shape model using kernel PCA. In *Proceedings of the 10th British Machine Vision Conference*, 1999.

[40] M. Rousson, A. Khamene, M. Diallo, J. C. Celi, and F. Sauer. Constrained surface evolutions for prostate and bladder segmentation in CT images. In *Computer Vision for Biomedical Image Applications*, 2005.

[41] B. W. Silverman. *Density estimation for statistics and data analysis*. Chapman and Hall, 1986.

[42] M. H. P. Smitsmans, J. W. H. Wolthaus, X. Artgnan, J. de Bois, et al. Automatic localization of the prostate for on-line or off-line image-guided radiotherapy. *International Journal of Radiation Oncology, Biology, Physics*, 60(2), 2004.

[43] L. Staib and J. Duncan. Model-based deformable surface finding for medical images. *IEEE Transactions on Medical Imaging*, 15(5):720–731, 1996.

[44] A. Tsai, A. Yezzi, W. Wells, C. Tempany, D. Tucker, A. Fan, W. E. Grimson, and A. Willsky. A shape-based approach to the segmentation of medical imagery using level-sets. *IEEE Transactions on Medical Imaging*, 22(2), 2003.

[45] G. Unal and G. Slabaugh. Coupled PDE for non-rigid registration and segmentation. In *Proceedings of IEEE Conference on Computer Vision and Pattern Recognition*, 2005.

[46] F. Wang, B. Vemuri, and A. Rangarajan. Groupwise point pattern registration using a novel CDF-based Jensen-Shannon Divergence. In *2006 IEEE Computer Society Conference on Computer Vision and Pattern Recognition*, 2006.

[47] W. Xu, S. Amin, O. Haas, K. Burnham, and J. Mills. Contour Detection by Using Radial Searching for CT Images. 4th Int. In *IEEE EMBS Special Topic Conf. on Information Technology Applications in Biomedicine*, pages 346–349, 2003.

[48] A. Zaim and J. Jankun. A Kohonen Clustering based Approach to Segmentation of Prostate from TRUS Data using Gray-Level Co-occurrence Matrix. In *Computer Graphics and Imaging: Eighth IASTED International Conference Proceedings*, 2005.

[49] R. Zwiggelaar, Y. Zhu, and S. Williams. Semi-automatic segmentation of the prostate. In *IbPRIA*, 2003.